Electromagnetic Time-Reversal Imaging in Changing Media: Experiment and Analysis

Dehong Liu, Sathya Vasudevan, Jeffrey Krolik, [1]Guillaume Bal and Lawrence Carin
Department of Electrical and Computer Engineering
Duke University
Durham, NC 27708-0291
lcarin@ee.duke.edu

[1] Department of Applied Physics & Applied Mathematics
Columbia University
New York, New York

Abstract **–** An experimental study is performed on electromagnetic time reversal in highly scattering environments, with a particular focus on performance when environmental conditions change. In particular, we consider the case for which there is a mismatch between the Green's function used on the forward measurement and that used for time-reversal inversion. We examine the degradation in the time-reversal image with increasing media mismatch, and consider techniques that mitigate such degradation. The experimental results are also compared with theoretical predictions for time reversal in changing media, with good agreement observed.

I. Introduction

Time reversal is a technique that is based on the principle of reciprocity [1]. In particular, assume a source emits radiation that propagates through a complex media to a set of receiving antennas. The data that arrives early in time at a given receiver implicitly travels a shorter distance than data that arrives later in time. By reversing the received waveforms in time, and emitting them from their respective reception points, the data that traveled a longer distance is emitted early, and the data that traveled a shorter distance is emitted later, and all of the energy arrives at the original source in unison, approximately recreating the original excitation. In the above discussion we have assumed that the medium is lossless. Further, the original source is not recreated exactly after time reversal, because in practice a finite set of receiver/source antennas are used.

While the concept of time reversal is simple, a direct result of reciprocity, it has important implications. For example, in conventional imaging the focusing resolution is limited by the size of the antenna aperture (for an antenna array) [2]. However, in a complex propagation medium, characterized by multiple paths from the original source to the receiving elements, time reversal may have an *effective* aperture [3,4] that is much larger than that of the physical array aperture and acts as a filter that increases with the number of available paths [5,6]. This phenomenon has been termed "superresolution" [4]. Interestingly, the more complex the media the more paths are manifested from a source to the multiple receivers, thereby enhancing superresolution refocusing quality. However, while resolution quality may be enhanced by increased media complexity, one also typically observes a reduction in the energy refocused at the original source [4,5,6] (the complex media yields highly scattered waves, most of which are not observed by the antennas).

Time reversal has been demonstrated experimentally in an extensive set of ultrasonic and acoustic measurements [7-13], as well as in recent electromagnetic studies [14,15]. Time reversal examined in this previous work consists of two steps: (i) a source emits a pulse of radiation from a given point in a complex propagation environment, with the data observed at a set of receiving antennas; and (ii) the time-domain data at each of the receiver elements are reversed and synchronously re-radiated from the respective source-receiver antennas. If the media through which steps (i) and (ii) are executed are the same, the time-reversal phenomena is well established [7], and refocusing is observed at the original source point. A question arises as to focusing quality when there is a mismatch between the environments considered in steps (i) and (ii). This mismatch may be manifested in several ways. For example, there may be time-varying elements within the media, yielding a change in the Green's functions associated with steps (i) and (ii). Consider, for example, localization of an electromagnetic source within a building in which people may be moving. As another example, in many applications step (ii) may be performed computationally rather than experimentally. In particular, if a source in step (i) emits radiation, which we wish to localize (image) using step (ii), one requires a propagation model [15] to implement (ii). In this context there will often be uncertainties

in knowledge of the parameters of the media, or limitations of the accuracy of the numerical model with which step (ii) is implemented. For these reasons it is of interest to examine how differences in the Green's functions used for steps (i) and (ii) deteriorate time-reversal refocusing quality. Work of this type has been examined experimentally in acoustics [8,17] and ultrasonics [10], as well as in theoretical studies [6]. For example, in [11-13] time-reversal refocusing quality was examined in an ocean channel, as the acoustic medium (sound-speed profile) changed with time. In the work presented here we consider such phenomenon in an electromagnetic setting, with a more-controlled measurement, allowing comparisons with theoretical predictions [6]. In particular, theory predicts that the strength of the refocused signal is an increasing function of the correlation of the two underlying media between the forward and backward stages of the time reversal experiment.

We may seek to generalize time reversal, particularly when there is uncertainty in the medium associated with step (i). Addressing the imaging problem, rather than numerically implementing step (ii) through a *single* (fixed) media, which may be different from that actually used in step (i), we may perform this step using an ensemble of media (*i.e.*, a media subspace, with the idea that the actual media from step (i) may be in the subspace, but without requiring knowledge of the exact/precise media associated with step (i)). For example, we may use an *average* Green's function for step (ii), with averaging performed over an ensemble of Green's functions corresponding to a set of (distinct) media related to the particular media for which step (i) was performed. Alternatively, one may perform an eigen-based principal components analysis (PCA) [19] on an ensemble of Green's functions for different media in step (ii), with use of the principal eigenvector(s) when imaging. We examine these techniques for electromagnetic source localization in changing and uncertain media.

The remainder of the paper is organized as follows. In Sec. II we describe the experimental system used to perform the electromagnetic measurements considered. Example imaging results are presented for the case of matched media between steps (i) and (ii) discussed above, demonstrating the superresolution phenomenon. Results are

presented as a function of the physical aperture size and as a function of the frequency bandwidth employed, and comparisons are made to theoretical predictions. The problem of mismatched media is examined in Sec. III, with a carefully performed set of controlled measurements. The results of these measurements are also compared with theoretical predictions. Imaging and source localization are considered in Sec. IV, using techniques that account for the uncertainty of the Green's function employed in step (ii). An extensive set of imaging results are presented, with the different techniques compared. Conclusions are provided in Sec. V.

II. Experimental Configuration and Matched Media

A. Details of measurements

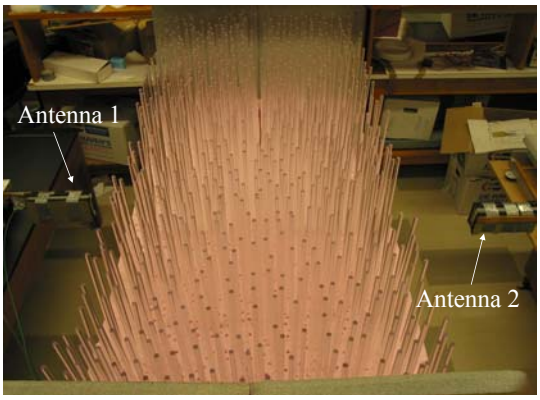

Figure 1. Dielectric rod experimental setup used in experimental time-reversal studies. The two antennas are moved using precision stepper motors. The length of the domain in the horizontal direction is 1.2 m, and it is 2.4 m in the vertical direction (of this photo).

Electromagnetic time reversal (ETR) measurements are performed using a vector network analyzer. These time-reversal studies extend many previous measurements performed with acoustic and ultrasonic systems [7-13], as well as recent electromagnetic studies [14,15]. The measurements are performed with Vivaldi antennas, over the 0.5-10.5 GHz band. The electric fields are polarized vertically. Low-loss dielectric rods of 1.25 cm diameter, 0.6 m length, and with approximate dielectric constant $\varepsilon_r = 2.5$ are situated with axes parallel to the direction of the electric fields. As indicated in Fig. 1, a total of 750 rods are considered, configured randomly, with an average inter-rod spacing of 6.5 cm (between rod axes). The rods are situated in a domain 1.2 m long and 2.4 m wide, with the rods embedded at the bottom in styrofoam ($\varepsilon_r \approx 1$); the 2.4 m width is employed to minimize edge effects in the measurements, as detailed below. A top view of the geometry is shown in Fig. 2. The

1.2×2.4 m^2 rod domain is composed of six distinct and contiguous rod sections (see Fig. 2), each 2.4 m wide and 20 cm long. Multiple rod-placement realizations may be manifested by interchanging the positions of the six styrofoam-supported subsections. The antennas are situated in a plane bisecting the midpoint of the rods.

The measurements are performed with two antennas, one used for transmission and the other for reception. Multiple antenna positions are realized using precision stepper motors. The transmitting antenna, on one side of the domain (see Fig. 2), is placed at $M \times M$ positions, with inter-grid spacing $\Delta_x = \Delta_y = 2.5$ cm. On the other side of the domain the receiver antenna is moved to N positions along a linear aperture, with inter-element spacing $\Delta = 2.5$ cm.

Let the transmitting-antenna location be represented as $\boldsymbol{r}_m$, for m=1, 2, …, M^2, and the receiving antenna is placed at $\boldsymbol{r}_n$, for n=1, 2, …, N. These NM^2 measurements constitute the data $G_k(\omega, \boldsymbol{r}_n, \boldsymbol{r}_m)$, where ω represents the angular frequency. As indicated above the positions of the six contiguous styrofoam sections are interchanged to constitute different media realizations, the kth of which defining $G_k(\omega, \boldsymbol{r}_n, \boldsymbol{r}_m)$.

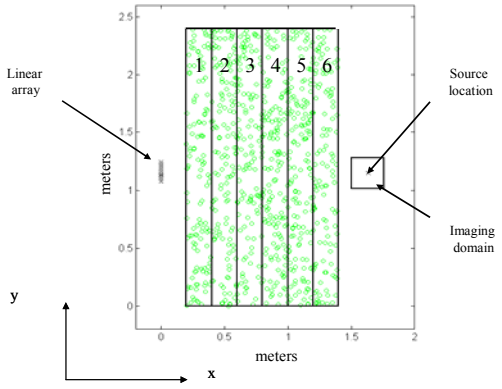

Figure 2. Top schematic view of the rods in Fig. 1. The rods are decomposed into six regions, with the rods in each region held together at the bottom via styrofoam. Different media instantiations are implemented by interchanging the positions of the six rod regions.

The center of the $M \times M$ domain is defined as the source position $\boldsymbol{r}_s$, and the fields measured on the linear aperture due to this source are $S_k(\omega, \boldsymbol{r}_n) = G_k(\omega, \boldsymbol{r}_n, \boldsymbol{r}_m = \boldsymbol{r}_s)$. An electromagnetic time-reversal (ETR) space-time image is computed using the measured Green's functions as

$$I_{jk}(t, \boldsymbol{r}_m) = \sum_{n=1}^{N} \int_{\omega_{BW}} d\omega \; W^*(\omega) S_j^*(\omega, \boldsymbol{r}_n) G_k(\omega, \boldsymbol{r}_n, \boldsymbol{r}_m) \exp(-i\omega t) \qquad (1)$$

where the Fourier integral is performed over the system bandwidth ω_{BW}, the symbol * denotes complex conjugate, and $W(\omega)$ is the window function used to weight (shape) the source excitation. While $S_j(\omega, \boldsymbol{r}_n)$ and $G_k(\omega, \boldsymbol{r}_n, \boldsymbol{r}_m)$ are both measured, the final image defined by (1) is synthesized; we typically consider the image manifested at t=0. We may observe ETR quality when the forward and inverse measurements are matched (j=k) and when there is a mismatch ($j \neq k$).

B. Time-reversal imaging for matched media: effective aperture

In the first set of results we consider j=k, and address image quality as a function of the bandwidth and aperture size considered. All images are shown at the $M \times M$ imaging points, at t=0. Ideally we expect spatial focusing at the center source location. In these examples M=13, and in the initial case N=5. A representative example image is presented in Fig. 3, for which tight spatial focusing is observed at the source location.

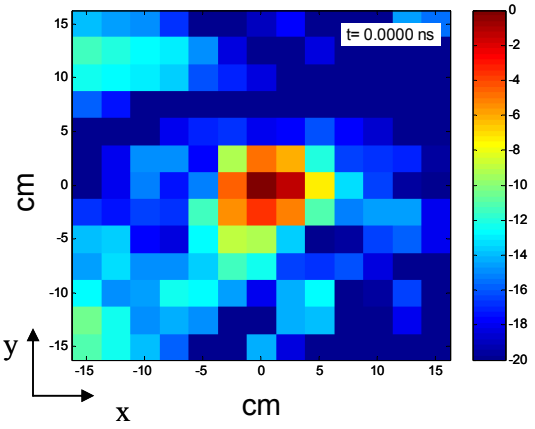

Figure 3. Time reversal focusing of a single antenna source via an N=5 element linear array. The color scale is in dB. The results use the full 0.5-10.5 GHz bandwidth.

An important issue of interest concerns time-reversal image stability [18]. This measure of stability addresses the case $I_{jj}(t=0, \boldsymbol{r}_m)$, for which the Green's functions in the

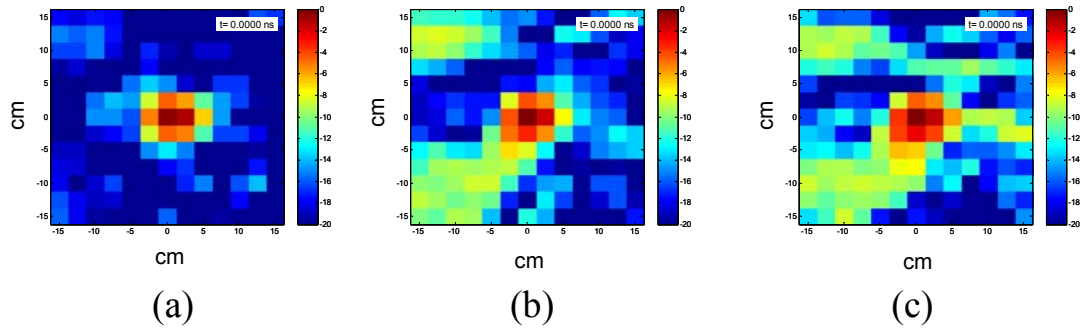

Figure 4. As in Fig. 3, but for N=9, N=3 and N=1 linear elements. (a) N=9, (b) N=3, (c) N=1

forward and inverse components of time reversal (steps (i) and (ii), respectively, from the Introduction) are matched; the issue of stability [18] considers the variation in $I_{jj}(t=0,\boldsymbol{r}_m)$ across different j (here, for different ordering of the six rod subsections reflected in Fig. 1), with theory indicating that this variation should be weak. Stability is addressed in detail in Sec. IID below.

The multi-path manifested from the rods yields an effective linear aperture that is larger than that of the physical N-element linear receiver array [4], manifesting "superresolution". It is of interest to examine this phenomenon in the context of the present measurements. Using the full-band data (0.5-10.5 GHz) the measured cross-range resolution is approximately 7.5 cm, with approximately 10 cm resolution in down-range. For a homogeneous medium, the anticipated cross-range resolution is $R_c = \lambda L / a$, where λ is the wavelength, a is the real linear aperture length, and L is the distance from the aperture center to the imaging point. If we consider a free-space medium, and center frequency 5.5 GHz, a real aperture a=10 cm (for N=5), and length L=1.5 m, the optimal free-space cross-range resolution is R_c=81.75 cm; Fig. 3 demonstrates the significant improvement in cross-range resolution manifested by the rod-induced multipath.

To further assess the superresolution phenomenon, in Fig. 4 we present example time-reversal imaging results (at t=0) for N=9, N=3 and N=1 receiver elements. The results for N=5 and N=9 elements are comparable, with only a slight degradation for the case of N=3. It is interesting to note the well-focused imaging results even for N=1, corresponding to no *physical* aperture. The case of N=1 refocusing antennas underscores the significant *effective* aperture manifested by this highly-scattering environment.

C. Time-reversal imaging for matched media: effect of bandwidth

An important observation from our measurements is the dependence of the ETR image quality on the system bandwidth *and* the absolute frequencies employed, as was the case for acoustic waves [1,7]. For example, in . 5 we consider N=5 linear elements and a fixed bandwidth of 2.5 GHz. However, the absolute frequencies considered in Figs. 5(a)-(c) are

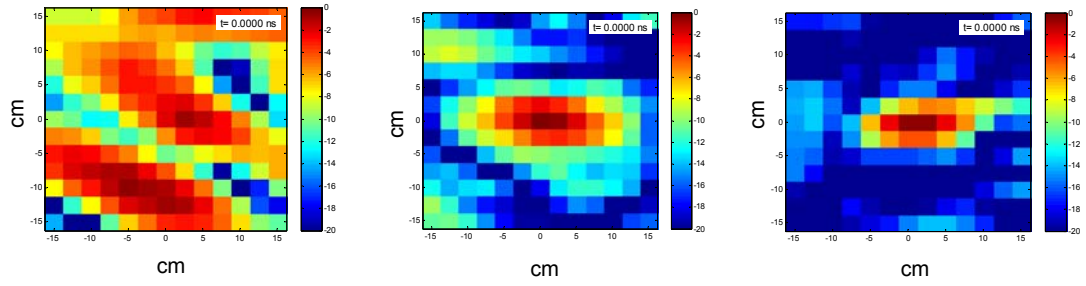

Figure 5. Time reversal focusing of a single antenna source via an N=5 element linear array. The color scale is in dB. Results are shown using a constant bandwidth of 2.5 GHz, but with absolute bandwidths of 0.5-3 GHz, 2.5-5 GHz and 5-7.5 GHz. (a) 0.5-3 GHz, (b) 2.5-5 GHz, (c) 5-7.5 GHz.

respectively 0.5-3 GHz, 2.5-5 GHz and 5-7.5 GHz. The 5-7.5 GHz results in Fig. 5(c) are only slightly less well focused than the full-band results in Fig. 3. However, much weaker focusing is observed for the bandwidth considered in Fig. 5(a). This is attributed to the fact that, at 3 GHz, the wavelength is relatively large relative to the inter-rod spacing and to the overall distance of propagation, and therefore the rods act as an effective mixture medium, rather than a highly multi-scattering environment. This lack of multi-path undermines the aforementioned *effective* increase in the aperture size. However, the multipath increases for the 5-7.5 GHz data, yielding multi-path-induced superresolution.

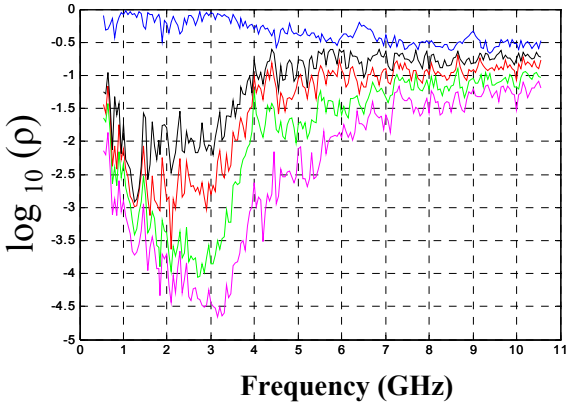

Figure 6. Logarithm of the five eigenvalues ρ of the time-reversal operator, as a function of frequency, for the data considered in Fig. 5.

To demonstrate the frequency-dependent properties of the dielectric-rod medium, let $\boldsymbol{v}_j(\omega)$ represent an $N\times 1$ vector, with nth element defined by $S_j(\omega,\boldsymbol{r}_n)$. The $N\times N$ time-reversal array matrix [20] is defined as $\boldsymbol{V}(\omega)=\sum_{j=1}^{J}\boldsymbol{v}_j(\omega)\boldsymbol{v}_j(\omega)^H$, where we have summed over 24 realizations of the media (24 different orderings of the rods subsections in Fig. 1) and superscript H denotes complex

transpose. In Fig. 6 we plot the N=5 eigenvalues of $\boldsymbol{V}$ as a function of frequency (for N=5 linear receiver elements). If the medium is relatively weakly scattering, then each $\boldsymbol{v}_j(\omega)$ will be similar with small (random) variation, and one would expect a single principal eigenvalue, representative of the single source at $\boldsymbol{r}_s$. If the medium is highly scattering, waves will be incident upon the N-element receiver array from multiple angles, and the rank of $\boldsymbol{V}$ will increase. One notices two distinct regions in Fig. 6. Up to approximately 4 GHz there is one principal mode, implying that in this frequency range the waves realize relatively weak multipath, and the rods constitute a relatively weak-scattering random media. Above 4 GHz the five eigenvalues are similar in magnitude, implying that $\boldsymbol{V}$ is full rank, and that the medium is highly scattering. As indicated in the previous paragraph, the highly-scattering character of the waves above 4 GHz is beneficial to time reversal, in that it yields an increased effective aperture and superresolved imaging resolution.

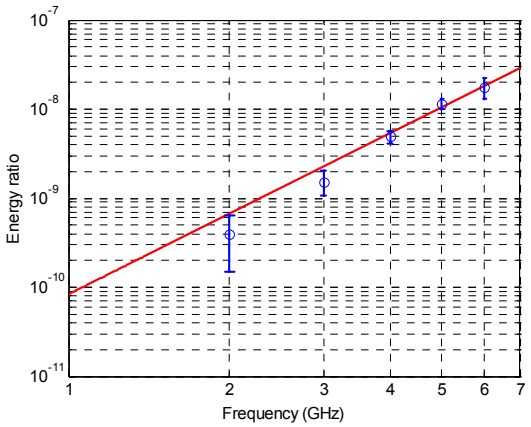

Figure 7. Mean focusing energy at source point, normalized by energy in excitation, as a function of frequency. The error bars represent the standard deviation across 24 realizations of the media, realized by interchanging the rod regions in Fig. 2.

D. Frequency dependence of focusing energy, and image stability

Theoretical studies in the Rayleigh scattering regime (scatterers of small diameter compared to wavelength) predicts that the ETR focusing intensity should increase as the third power of frequency in two space dimensions and as the fourth power of frequency in three dimensions [6]. To consider this issue, we considered the ratio of energy focused at the original source location, normalized by the source energy, as a function of frequency. The experimental results in Fig. 7 confirm the theoretical predictions (for this approximately two-dimensional system), demonstrating a frequency dependence of f^3. The error bars in Fig. 7 correspond to different realizations of the media (as discussed in

Sec. II, manifested by interchanging the six rod regions, as reflected in Fig. 2). To compute the results in Fig. 7, full-band ETR imaging was performed, yielding a time-dependent signal for the data imaged via time reversal to the original source location. A Fourier transform was performed of this waveform, and the energy was normalized to the strength of the excitation energy, as a function of frequency.

We also note that the error bars reflected in Fig. 7, corresponding to variation in $I_{jj}(t=0,\boldsymbol{r}_m)$ for 24 distinct manifestations of the intervening rod media, are relatively tight (little variation across different media realizations). This observation is consistent with previous studies that predict a high degree of stability [18] in the time-reversal image quality, for different media realizations (assuming the media used in the forward and inverse steps is the same).

III. Controlled Mismatched Media and Comparisons to Theory

The following measurements are motivated by theoretical studies of time-reversal in changing media. Specifically, the measurements attempt to replicate the conditions addressed in [15]. In Fig. 8 we consider the 2.4 m wide and 1.2 m long media discussed above. A source on the right of the domain emits energy that is observed at the N=5 linear elements at left (the source is at the midpoint of the 2.4 m rod-region width). The data are time reversed (phase conjugated) and the measured Green's function over the square imaging domain is used to constitute an ETR image at t=0, as in (1). We now consider how the ETR image changes if the time-reversed fields are imaged using a Green's function corresponding to the shifted media in Fig. 8 (now $j \neq k$ in (1)). By incrementally increasing the shift through which ETR imaging is performed (Fig. 8), we perform a controlled examination of how ETR refocusing quality deteriorates as the mismatch (shift distance) increases between the original and shifted (Fig. 8) media used for imaging. Note that the use of a 2.4 m wide media was necessitated by edge effects observed when executing such shifting when the media was only 1.2 m wide (placement of the original source in the middle of the 2.4 m domain was also performed to minimize edge effects caused by the finite-width medium).

The ETR images at t=0 are shown in Fig. 9, as a function of shift distance. The white circle in each sub-image of Fig. 9 corresponds to the physical location of the *actual* original source, with respect to which the imaging domain is shifted (see Fig. 8). Considering Fig. 9, we note that the down-range resolution (along the horizontal direction of the figures) is preserved as the media is shifted; however, with increasing shift distance the cross-range localization (vertical direction) is lost. It is interesting to examine the imaging amplitude in the *center* of each of the shifted imaging domains (in the center of each of the subimages in Fig. 9). The energy in the center of the imaging domain appears to oscillate between strong and weak amplitudes, with increasing shift. As now discussed in further detail, this oscillation is predicted to be of the form of a zeroth-order Bessel function [6].

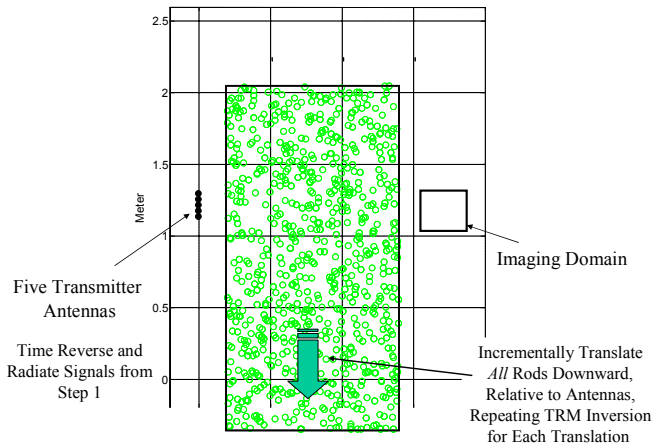

Figure 8. Examination of time reversal imaging in changing media, with change manifested via a shift in the media. In Step 1 a single antenna is placed in the center of the imaging domain at right, and the radiated fields are observed on the five antennas at left. These fields are time reversed and reradiated into the domain, with the fields from this process observed in the imaging domain. Imaging results are considered as a function of the relative shift in the media, considered within the time-reversal stage.

In the diffusion regime, it has been predicted that the amplitude at the center of the imagery domain, for shifts of the type considered in Fig. 9, should vary as $J_o(k\tau)$ where τ is the spatial shift and k is the wavenumber. A qualitatively similar result is predicted in the radiative transfer regime. In Fig. 10 we plot the energy observed at the center of each image, as a function of the shift between the media considered in step (i) and step (ii) of the time-reversal process. In addition, the results in Fig. 10 are presented as a function of the bandwidth used when performing time reversal. In Fig. 11 we plot the magnitude of the excitation

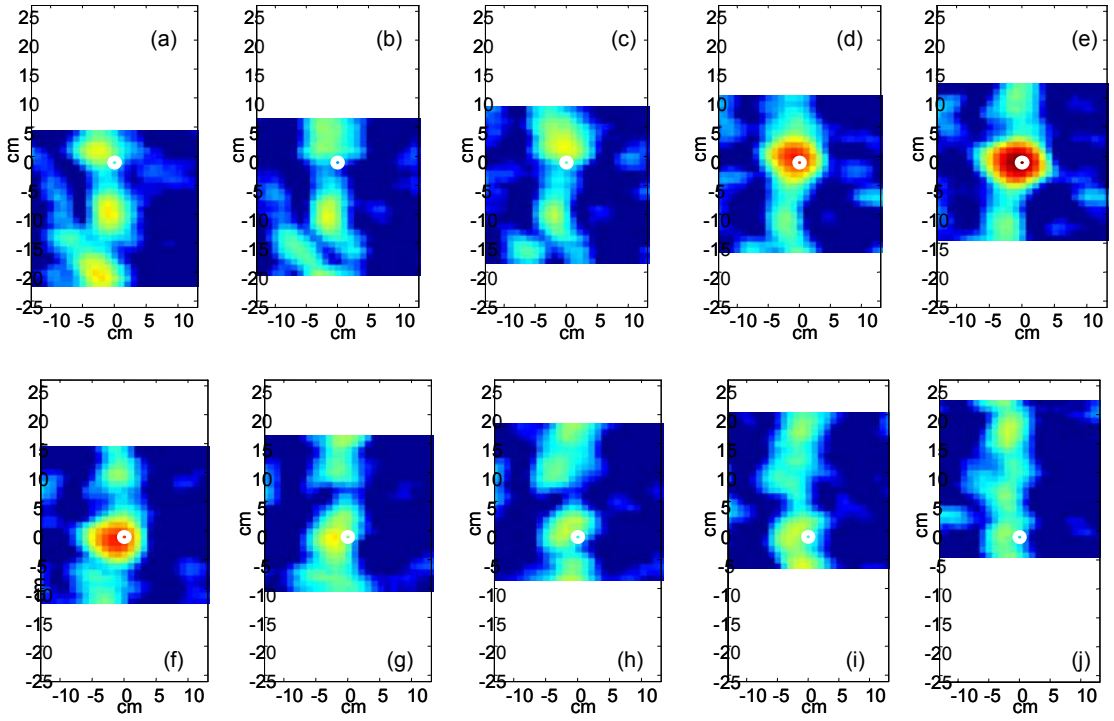

Figure 9. Time reversal image as a function of shift in the media (see Fig. 8). The position of the original source is shown with the white circle. (a) -8 cm shift, (b) -6 cm, (c) -4 cm, (d) – 2 cm, (e) 0 cm, (f) 2 cm, (g) 4 cm, (h) 6 cm, (i) 8 cm, (j) 10 cm

window used in (1), $|W(\omega)|$. Considering $|W(\omega)|$, the strongest energy in one of the subbands considered in Fig. 11 occurs at the respective peak energy (*e.g.*, for the 0.5-1 GHz subband, the greatest energy is at 1 GHz). Using this understanding, for a given subband in Fig. 10, we perform comparisons to $J_o(k\tau)$ for the wavenumber k associated with the respective peak frequency.

Using $J_o(k\tau)$, the first null in the predicted energy at the center of the imaging domain should occur at shifts of 12 cm, 8 cm, 6 cm and 4.8 cm, for respective (peak) frequencies of 1 GHz, 1.5 GHz, 2 GHz and 2.5

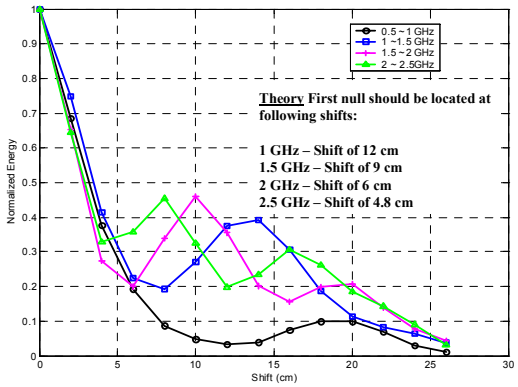

Figure 10. Normalized energy at the center of each subimage in Fig. 9, as a function of sensor bandwidth. The theoretical predictions for the position of the first null are tabulated in the inset.

GHz. By considering Fig. 11, we note excellent agreement between our measured results and the predictions based on the theory in [6]. A qualitative behavior of the refocused intensity proportional to $J_o(k\tau)$ is not a characteristic of the diffusion regime; for instance it approximately holds in the less scattering radiative transfer regime [6]. We have also stressed that frequencies below 4 GHz were weakly scattering. However it does demonstrate that multiple scattering is responsible for the refocused signal, for in homogeneous medium, the refocused energy would not depend on the shift τ. Moreover it indicates that loss of correlation between the two media of the two stages of the time reversal experiment induces reduction in refocused signal strength. Knowledge of the exact Green's function is therefore quite important to maximally benefit from the refocusing properties of time reversed waves.

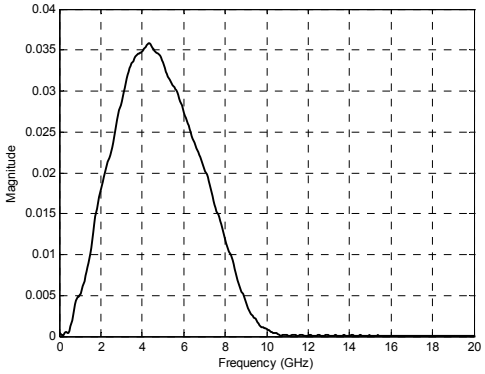

Figure 11. Spectrum of the waveform used in the time-reversal experiments.

IV. Imaging in Changing Media

The results in Sec. III considered controlled changes (shifts) in the media used for steps (i) and (ii) of time reversal (the forward and inverse components, respectively), to perform a comparison with theoretical predictions. It was observed that substantial deterioration of the time-reversal image is manifested as the shift distance (change in media) increases. In this section we examine changes to the time-reversal imaging procedure, with the goal of enhancing imaging quality and realize robustness to uncertainty about the Green's function associated with step (i). In particular, we make the assumption that while the precise (specific) Green's function used in step (i) may be unknown, we may have an ensemble of Green's functions available, representative of media with similar statistics. Different media are constituted by interchanging the positions of the six regions in Fig. 1. Below we first summarize the imaging techniques considered, followed by experimental results that demonstrate their relative performance.

A. Imaging with mismatched Green's function

We consider image quality $I_{jk}(t=0,\boldsymbol{r}_m)=\sum_{n=1}^{N}\int_{\omega_{BW}} d\omega\; S_j^*(\omega,\boldsymbol{r}_n)G_k(\omega,\boldsymbol{r}_n,\boldsymbol{r}_m)$ for $j\neq k$, addressing the problem for which there is a *completely* distinct arrangement of the six regions for cases *j* and *k* (see Fig. 2). Specifically, for the $j\neq k$ cases considered here there is *no* overlap for *any* of the six rod subsections with respect to media realizations *j* and *k* (complete mismatch). The image is computed using the discrete sampled frequencies as

$$I_{jk}(t=0,\boldsymbol{r}_m)=\sum_{n=1}^{N}\boldsymbol{s}_j^H(n)\boldsymbol{g}_k(n,m) \qquad (2)$$

where $\boldsymbol{s}_j(n)$ is an $N_F\times 1$ column vector representing the frequency dependence of $S_j(\omega,\boldsymbol{r}_n)$, $\boldsymbol{g}_k(n,m)$ is an $N_F\times 1$ column vector representing the frequency dependence of $G_k(\omega,\boldsymbol{r}_n,\boldsymbol{r}_m)$, N_F is the number of frequencies considered, and superscript *H* represents conjugate transpose.

As discussed in the Introduction, when performing imaging, step (ii) of time reversal is performed computationally, using either a measured or computed Green's function. When precise knowledge of media *j* is unavailable or cannot be modeled with full accuracy, then media *k* associated with $G_k(\omega,\boldsymbol{r}_n,\boldsymbol{r}_m)$ is mismatched to the forward measurement $S_j(\omega,\boldsymbol{r}_n)$. Below we consider alternative means of addressing an imperfect representation of media *j*, rather than simply computing $I_{jk}(t=0,\boldsymbol{r}_m)$ for $j\neq k$.

B. Averaged Green's function

Assume we have measured data $S_j(\omega,\boldsymbol{r}_n)$ from the linear array of receivers, corresponding to the *j*th realization of the media (placement of the six rod subsections). Further, assume that the particular media (Green's function) associated with this *j*th

example is unknown. However, we may have access to the *statistics* of the Green's function. Specifically, assume access to Green's functions from K realizations of the media (K realizations of the six rod subsections in Fig. 2), each of which is *entirely* distinct from the jth realization referenced above (as discussed above). If these K Green's functions are denoted $G_k(\omega, \boldsymbol{r}_n, \boldsymbol{r}_m)$, for k=1, …,K, then one simple idea would be to perform imaging using the average Green's function

$$G_{AVG}(\omega, \boldsymbol{r}_n, \boldsymbol{r}_m) = \frac{1}{K} \sum_{k=1}^{K} G_k(\omega, \boldsymbol{r}_n, \boldsymbol{r}_m) \tag{3}$$

with the time-reversal image represented as

$$I_{j,AVG}(t=0, \boldsymbol{r}_m) = \sum_{n=1}^{N} \boldsymbol{s}_j^H(n) \boldsymbol{g}_{AVG}(n,m) \tag{4}$$

where $\boldsymbol{g}_{AVG}(n,m)$ is an $N_F \times 1$ column vector representing the frequency dependence of $G_{AVG}(\omega, \boldsymbol{r}_n, \boldsymbol{r}_m)$.

C. Subspace imaging

The MUltiple SIgnal Classification (MUSIC) algorithm [21] employs the "noise" subspace from multiple data measured using an antenna array. This approach is appropriate for source localization when multiple instantiations of the array data are available, for a given source; such a situation may be manifested by repeated measurement of data from a stochastic source [20]. In the problem considered here we only have a single set of data $S_j(\omega, \boldsymbol{r}_n)$, for one (the jth) realization of the source and media. Direct application of MUSIC is therefore inappropriate. However, as discussed below, we may exploit related eigen-subspace ideas.

For a given source and receiver point, again assume access to K examples of the Green's function, denoted $G_k(\omega, \boldsymbol{r}_n, \boldsymbol{r}_m)$, for k=1, …, K. Rather than taking the average of these K Green's functions (for K realizations of the media), we may perform a principal components analysis (PCA) [19], and project the measured data onto the principal Green's function eigenvectors. We perform an eigen decomposition of the $N_F \times N_F$ matrix

$$\boldsymbol{G}(n,m) = \sum_{k=1}^{K} \boldsymbol{g}_k(n,m)\boldsymbol{g}_k(n,m)^H \tag{5}$$

Let $\boldsymbol{e}_l(n,m)$ represent the lth eigenvector of (5). A PCA-based imaging result is represented as

$$I_{j,EIG}(t=0,\boldsymbol{r}_m) = \sum_{n=1}^{N}\sum_{l=1}^{L_p} \boldsymbol{s}_j^H(n)\boldsymbol{e}_l(n,m) \tag{6}$$

In the example results we have considered L_p=1 principal component.

D. Example imaging results

The measurements were performed as follows. The Green's function $G(\omega,\boldsymbol{r}_n,\boldsymbol{r}_m)$ was measured for N_{media}=24 realizations of the six rod subsections depicted in Fig. 2. For the jth of these realizations, there was a set Ω_j of $N_j < N_{media}$ *other* rod arrangements considered for which there was a *complete* mismatch in the order of the six rod regions.

When considering the technique in Sec. IVA for media j, I_{jk} was calculated separately for all media $k \in \Omega_j$; consequently, for each media j we compute N_j distinct images I_{jk}. For the techniques in Secs. IVB and IVC, a single image is computed for each of the N_{media} media arrangements. Specifically, for $I_{j,AVG}$ the average Green's function $\boldsymbol{g}_{AVG}(n,m)$ was computed using the N_j media in Ω_j; for $I_{j,EIG}$ the principal component $\boldsymbol{e}_1(n,m)$ was also computed using the N_j media in Ω_j. We first present qualitative results based on these imaging techniques, followed in Sec. IVE by quantitative results. In these examples a total of N_{media}=24 media were considered, and for each media j on average N_j=10 (the minimum was N_j=6).

In Fig. 12(a) a representative image is performed using traditional time reversal as in (2), for which the Green's functions used for the forward and inverse parts of time reversal are entirely distinct – corresponding to (2). Figures 12(b) as 12(c) present representative results for $I_{j,EIG}(t=0,\boldsymbol{r}_m)$ and $I_{j,AVG}(t=0,\boldsymbol{r}_m)$, respectively, for which generally good imaging is observed. The improved results of Figs. 12(b) and 12(c) *vis-à-vis* Fig. 12(a) is expected, given that the former employ more information (the latter two both use an

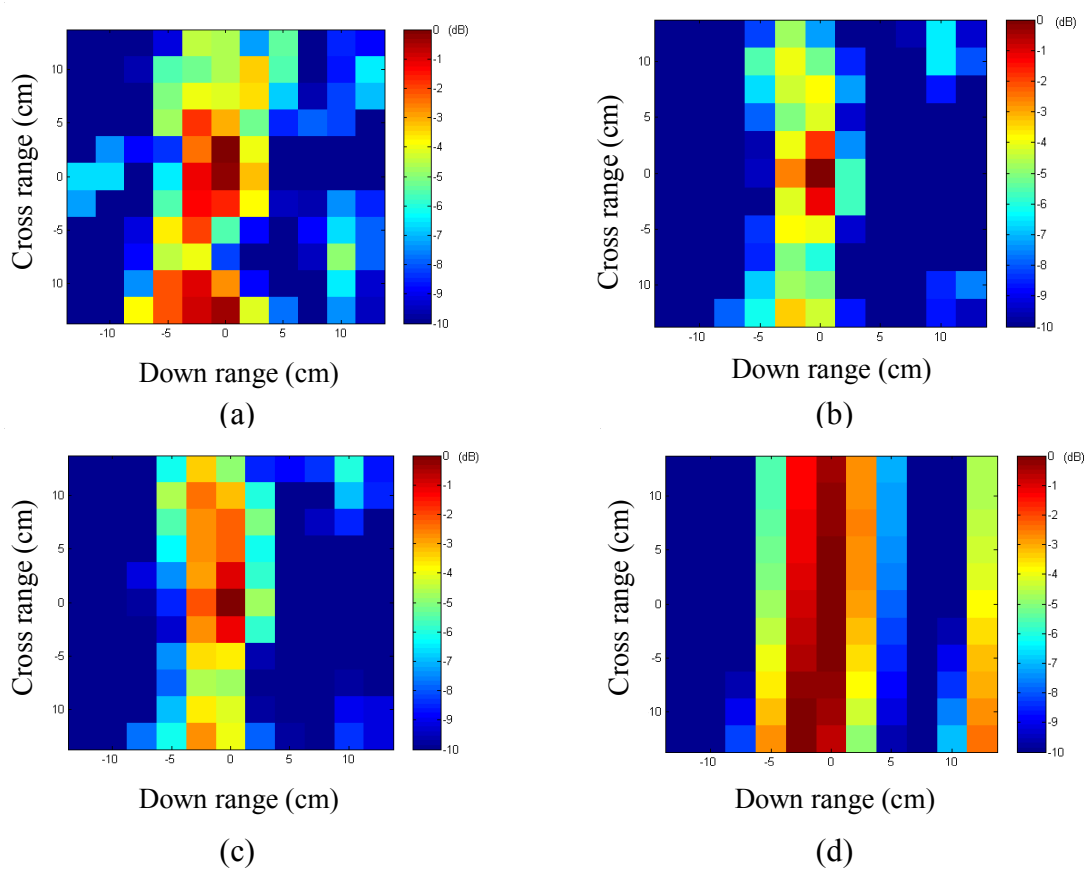

Figure 12. Typical time-reversal images for the case in which there is a complete mismatch between the Green's function associated with the forward and inverse phases of time reversal. Results are on a 10 dB scale. (a) Using mismatched Green's function, (b) using an eigen Green's function, (c) using an average Green's function, (d) using the free-space Green's function.

ensemble of Green's functions, while in Fig. 12(a) a *single* mismatched Green's function is employed). However, we underscore that each of Green's function employed in Figs. 12(a), 12(b) and 12(c), for computation of the average and eigen Green's functions, are entirely distinct from media j associated with forward measured data $S_j(\omega,\boldsymbol{r}_n)$. As a reference, in Fig. 12(d) we show results for which the Green's function $\boldsymbol{g}_k(n,m)$ in (2)

corresponds to the free-space Green's function – for this case no cross-range resolution is observed.

F. Quantitative analysis of imaging results

As indicated above, numerous images of the form in Fig. 12 have been generated by varying the placement of the rod positions, as reflected in Fig. 2. It is therefore of interest to perform a quantitative analysis of all such images. Toward this end, consider Fig. 13, for which a square region is defined (corresponding to a contiguous 3×3 pixel region in image space, with pixels defined as in Fig. 12). The test statistic l used in this analysis is defined by the peak pixel amplitude within the inner box. If $l > T$ a target is declared as being within the 3×3 inner region, and if $l < T$ no target is declared (the actual target position is in the center of the image, as in Fig. 12). By varying the threshold T, from zero to $T > l_{\max}$ (the largest value of l within a given image), we yield the receiver operating characteristic (ROC) [22], representing the probability of detection as a function of the probability of false alarm (a false alarm is defined by declaring the presence of a source at a location for which there is in reality none). In Fig. 14 we plot the ROC curves for the imaging techniques considered in Fig. 12. We note that the techniques based on the average and eigen Green's functions (equations (4) and (6), respectively) yield comparable performance, while performance declines precipitously when considering a single mismatched Green's function or the free-space Green's function (the latter yielding the worst results). The results in Fig. 14 indicate that, while time reversal may work poorly when the imaging is performed with a *single* mismatched Green's function, significantly improved performance is realized if one uses information

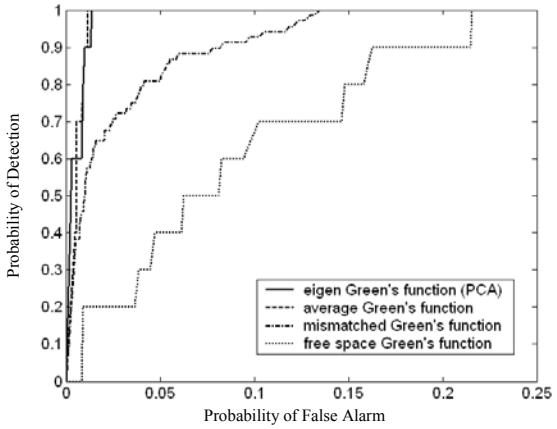

Figure 13. Receiver operating characteristic (ROC) averaged across multiple realizations of mismatched media, using the four imaging techniques reflected in Fig. 12.

in an *ensemble* of Green's function representative of that used in the forward measurement.

Let us mention that the performance obtained with the ensemble of Green's functions is significantly lower than what is obtained by using the exact Green's function. It is however significantly higher than that predicted by theory in the weak coupling regime, where fluctuations in the underlying structures are delocalized and small [6]. The exact mathematical average of the Green's functions over all possible realizations of a random media with given statistics should, according to theory in [6], not provide better refocusing than the Green's function in a homogeneous medium. That the results presented in this paper are significantly better than this prediction may have two origins. Firstly, the 24 realizations considered here are not completely statistically independent. Interchanging subsections 1 and 2 bears many similarities to a 20 cm shift in the medium. The results in Fig. 10 show that such shifts are still compatible with a sizeable refocused energy over a large frequency band and may thus be explained by theory [6]. Secondly, rods are by no means small fluctuations as the dielectric constant jumps from 1 in the air to 2.5 in the dielectric rods. Because 750 rods are packed on 2.88 m2, it is also quite likely that rods in stage two will end up very near locations of rods in phase 1. Such pairs of rods will have positive correlation for all frequencies larger that twice the inverse of the distance between the rods. We do not have a quantitative theory that explains such correlations. Yet our results seem to suggest that (i) correlations between the random media of both phases of time reversal are indeed sufficiently significant to generate a sizeable recompression at the source location, and (ii) that their effect is however statistically unstable as ensemble averages, either by averaging the Green's function or by projecting over the principal component to the realizations, provide more focused images than those obtained by a random Green's function.

V. Conclusions

Time-reversal imaging has been examined experimentally for electromagnetic source localization in highly scattering media. We initially addressed the well-known time-reversal behavior for the case in which the media employed in the forward and inverse steps are matched. These experiments confirmed theoretical predictions concerning time-reversal imaging stability, for the case in which the forward and inverse media are matched, but for different media realizations [6]. The experiments also confirmed the anticipated f^3 frequency dependence of the imaging amplitude in the Rayleigh regime [6], for the case of matched media.

After addressing the case of matched media, significant attention has been directed on the case for which the media employed in the forward and inverse steps are mismatched. The case of mismatched media for the inverse step is of relevance for changing media, as well as for numerical time-reversal imaging for which the exact media is unknown or cannot be modeled precisely.

In our first analysis of time-reversal imaging in changing media, we considered the special case for which the two media are shifted with respect to each other. While this is a special case, it is of particular interest because it allows us to address the accuracy of previous theoretical predictions [6]. In particular, in the diffusive regime it is predicted that the imaged amplitude should vary as $J_o(k\tau)$, where k represents the wavenumber and τ the spatial shift [6]; the experimental results considered here are in excellent agreement with theoretical predictions.

While the theory and experimental results indicate time-reversal imaging deterioration as media mismatch increases between the forward and inverse phases, we have also considered alternative techniques for the case in which the media employed in the forward phase is either unknown or may not be modeled precisely. Specifically, we have performed time-reversal imaging based on an average Green's function, computed using an ensemble of Green's functions; each Green's function in the ensemble corresponds to

a media completely distinct from that used in the forward step, but with similar statistics. A similar use of the ensemble of Green's functions was considered via an eigen analysis, analogous to principal components analysis (PCA) [16]. It was demonstrated that we often observe significantly improved time-reversal imaging quality based on either the average or eigen Green's function.

Concerning future research, in this study we have focused entirely on source localization. There is also interest in time-reversal imaging for the case of target scattering, for which the intervening multi-scattering environment is not known precisely, but potentially statistically (*e.g.*, for targets embedded in foliage). Such research will be the subject of future research.

References

[1] M. Fink, "Time-reversal of ultrasonic fields - Part I: Basic Principles," *IEEE Trans. Ultrason., Ferroelectr., and Freq. Control*, vol 39, pp. 555-566, 1992

[2] B. Steinberg, *Microwave Imaging Techniques,* New York: J. Wiley, 1991

[3] D.R. Jackson and D.R. Dowling, "Phase conjugation in underwater acoustics," *J. Acoust. Soc. of Amer.*, vol. 89, pp. 171-181,1990

[4] P. Blomberg, G. Papanicolaou, and H.K. Zhao, "Super-resolution in time-reversal acoustics," *J. Acoust. Soc. of Amer.*, vol. 111, pp. 230-248, 2002

[5] G. Bal and L. Ryzhik, "Time reversal and refocusing in random media," *SIAM Appl. Math.,* vol. 63 (5), pp. 1375-1498, 2003

[6] G. Bal and R. Verastegui, "Time reversal in changing environment," *Multiscale Model. Simul.* , vol. 2, pp. 639-661, 2004

[7] M. Fink, "Time reversed acoustics," *Physics Today*, 50, pp. 34-40, 1997

[8] A. Derode, P. Roux, and M. Fink, "Robust acoustic time reversal with high-order multiple scattering," *Phys. Rev. Lett.,* vol. 75, pp. 4206–4209, 1995

[9] P. Roux, B. Roman and M. Fink, "Time-reversal in an ultrasonic waveguide," *Appl. Phys. Letts.*, vol. 70, 1997

[10] J. de Rosny, A. Tourin, A. Derode, B. van Tiggelen and M. Fink, "The relation between time reversal focusing and coherent backscattering in multiple scattering media: a diagrammatic approach," *Phys. Rev. E*, vol. 70, 046601, 2004

[11] W.A. Kuperman, W.S. Hodgkiss, H.C. Song, T. Akal, C. Ferla, and D.R. Jackson**,** "Phase conjugation in the ocean: Experimental demonstration of an acoustic time-reversal mirror," *J. Acoust. Soc. Am.*, vol. 103, pp. 25-40, 1998.

[12] H.C. Song, W.A. Kuperman, W.S. Hodgkiss, T. Akial and C. Ferla, "Iterative time reversal in the ocean," *J. Acoust. Soc. Am.*, vol. 105, pp. 3176-3184, 1999.

[13] S. Kim, G.F. Edelmann, W.A. Kuperman, W.S. Hodgkiss, H.C. Song and T. Akal, "Spatial resolution of time-reversal arrays in shallow water," *J. Acoust. Soc. Am.*, vol. 110, pp. 820-829, 2001.

[14] G. Lerosey, J. de Rosny, A. Tourin, A. Derode, G. Montaldo and M. Fink, "Time reversal of electromagnetic waves," *Phys. Rev. Letts.*, vol. 92(19), 2004

[15] D. Liu, G. Kang, L. Li, Y. Chen, S. Vasudevan, W. Joines, Q. H. Liu, J. Krolik and L. Carin, "Electromagnetic time-reversal imaging of a target in a cluttered environment," *IEEE Trans. Antenna Propag.,* vol. 53, pp. 3058-3066, 2005

[16] J.L. Krolik, "The performance of matched-field beamformers with Mediterranean vertical array data," *IEEE Trans. Signal Process.*, vol. 44, pp. 2605-2611, 1996

[17] J.L. Krolik, "Matched-field minimum variance beamformaing in a random ocean channel," *J. Acoust. Soc. Amer.*, vol. 92, pp.1408-1419, 1992

[18] G. Bal, "On the self-averaging of wave energy in random media," *SIAM Multiscale Model. Simul.* , vol. 2, pp. 398-420, 2004

[19] A. Basilevsky, *Statistical Factor Analysis and Related Methods, Theory and Application*. New York: J. Wiley, 1994

[20] L. Borcea, G. Papanicolaou, C. Tsogka and J. Berryman, "Imaging and time reversal in random media," *Inverse Problems,* vol. 18, pp. 1247–1279, 2002

[21] F.K. Gruberic, E.A. Marengo and A.J. Devaney, "Time-reversal imaging with multiple signal classification considering multiple scattering between the targets," *J. Acoust. Soc. Am.*, 115, 2004

[22] T.D. Wickens, *Elementary Signal Detection Theory*. New York: Oxford University Press, 2002.